

Investigation of the effective interactions for the Emery model by the constrained random-phase approximation and constrained functional renormalization group

Xing-Jie Han,¹ Philipp Werner,² and Carsten Honerkamp³

¹*Institute for Theoretical Solid State Physics, RWTH Aachen University, D-52056 Aachen, Germany*

²*Department of Physics, University of Fribourg, 1700 Fribourg, Switzerland*

³*Institute for Theoretical Solid State Physics, RWTH Aachen University,
and JARA Fundamentals of Future Information Technology, D-52056 Aachen, Germany*

(Dated: October 28, 2020)

The effective interaction of downfolded low-energy models for electrons in solids can be obtained by integrating out the high energy bands away from the target band near the Fermi level. Here, we apply the constrained random-phase approximation (cRPA) and constrained functional renormalization group (cfRG), which can go beyond cRPA by including all one-loop diagrams, to calculate and compare the effective interactions of the three-band Emery model, which is often used to investigate cuprate high-temperature superconductors. At half band filling, we find that the effective interaction increases as the charge transfer energy (Δ_{dp}) increases and similar behavior is obtained as a function of the interatomic $2p$ - $3d$ interaction (U_{dp}). However, the effective interaction is more sensitive to Δ_{dp} than U_{dp} . For most of the parameter sets, the effective static interaction is overscreened in cRPA compared to cfRG. The low-energy models at half-filling are solved within dynamical mean-field theory (DMFT). The results show that despite the different static interactions, the systems with cRPA and cfRG interaction exhibit a Mott transition at similar values of Δ_{dp} . We also investigate the effective interaction as a function of doping. The cfRG effective interaction decreases as the electron number increases and displays a trend opposite to that of cRPA. Antiscreening is observed for the hole-doped case. For all the cases studied, the near-cancellation of the direct particle-hole channel is observed. This indicates that at least for the downfolding of the onsite interaction terms, methods beyond cRPA may be required.

I. INTRODUCTION

Tremendous progress has been made in understanding and predicting new materials with particular properties by *ab initio* methods based on density functional theory (DFT),¹ including recent advances in topological semimetals^{2,3} and superconductivity in the sulfur hydride systems.^{4,5} Despite the success of DFT for those weakly correlated materials, the method suffers from intrinsic difficulties and sometimes gives qualitatively wrong results for strongly correlated materials. For example, the insulating behavior of some transition metal oxides is not captured by DFT.^{6,7} In strongly correlated systems, the Coulomb repulsion between the low-energy electrons occupying the partially filled narrow bands in proximity to the Fermi level is comparable or larger than the bandwidth, and in such a situation the independent-particle picture of DFT breaks down. Meanwhile, most macroscopic properties of materials are mainly determined by those low-energy states near the Fermi level at low temperatures. Therefore, to accurately account for the low-energy correlation effects beyond the mean-field level, more sophisticated numerical methods aimed at the study of many-body model Hamiltonians, like the fluctuation exchange approximation (FLEX),^{8,9} Quantum Monte Carlo (QMC) methods^{10–12} and Dynamical Mean Field Theory (DMFT),^{13–15} have been employed to complement DFT calculations. The combination of DFT and DMFT has been extensively used to study correlated materials ranging from high-temperature superconductors to heavy fermion systems.^{16–18}

A crucial step in most of the DFT+DMFT calculations is the construction of low-energy effective Hamiltonians in the subspace of relevant states near the Fermi level, which contains the correlated d or f orbitals, starting from the complete Hilbert space. In this so-called downfolding process, the parameters of the low-energy effective Hamiltonians are derived by integrating out the high-energy degrees of freedom successively, in the spirit of renormalization group methods.¹⁹ While the downfolding concept is physically intuitive and straightforward, the parameter-free determination of the (partially) screened low-energy interactions still remains a major challenge and bottleneck for practical *ab initio* calculations.

To compute the screened Coulomb interaction for the low-energy effective Hamiltonians, a commonly used method is the constrained-random-phase approximation (cRPA).^{20,21} In cRPA, the partially screened Coulomb interaction between electrons in the low-energy subspace is frequency-dependent and is determined by $U(\omega) = [1 - vP_r(\omega)]^{-1}v$, where v is the bare Coulomb interaction and P_r is the particle-hole polarization function calculated by the RPA-type diagrams, excluding the contributions solely within the low-energy subspace. The latter is needed because polarization effects within the low-energy subspace are explicitly treated in the solution of the low-energy effective Hamiltonian. More specifically, at least one of the lines in the polarization particle-hole bubble P_r belongs to the high-energy sector. Although cRPA appears to be a big step forward and has been applied to calculate the screened Coulomb interactions for various materials and toy models,^{22–30}

both underestimations²³ and overestimations^{27–29} of the screening effects have been reported. Since many physical properties of strongly correlated materials are sensitive to small changes in U , especially near phase transition points, a better understanding of the limitations of cRPA is important for reliable parameter-free *ab initio* calculations and predictions.

Recently, the constrained functional renormalization group (cfRG) method^{32–35} has been proposed to go beyond cRPA by including all one-loop diagrams and vertex corrections. The cRPA can be recovered by only keeping the RPA-type diagrams. A multi-orbital Hubbard model which could be solved exactly using QMC has been studied to test the accuracy of cRPA and cfRG at the level of the effective one-band interaction after downfolding.³⁵ Significant corrections to cRPA were found and the overestimated screening effects in cRPA could be explained by the near-cancellation of certain loop corrections in cfRG. Furthermore, antiscreening effects, i. e. an enhancement of the bare interactions, were predicted by cfRG for the cases studied in Refs. 33–35, in contrast to the general suppression of the bare interactions by cRPA.

In this work, to further explore the differences between cRPA and cfRG, we use cRPA and cfRG downfolding schemes for the two-dimensional three-band Emery model³⁶ and calculate the effective interactions for the low-energy band using different model parameter sets. To further reveal the origin of the different results obtained by these two methods, the idea of channel decomposition is used. The effects of the resulting frequency-dependent cfRG and cRPA interactions are illustrated by solving the corresponding low-energy single band models using DMFT.

The rest of the paper is organized as follows. In Sec. II we introduce the Emery model and present the cRPA and cfRG downfolding schemes. Section III presents the cRPA and cfRG calculations for the effective interactions in the target band. The DMFT results are discussed in Sec. IV, and the paper is summarized in Sec. V.

II. MODEL AND METHODS

A. Model Hamiltonian

Compared to the extensively investigated one-band Hubbard model, a more realistic model to describe the physics of cuprates is the three-band Emery model, which includes the copper $3d_{x^2-y^2}$ orbital and the ligand oxygen $2p_x$ and $2p_y$ orbitals for the CuO_2 planes. It is defined by the Hamiltonian

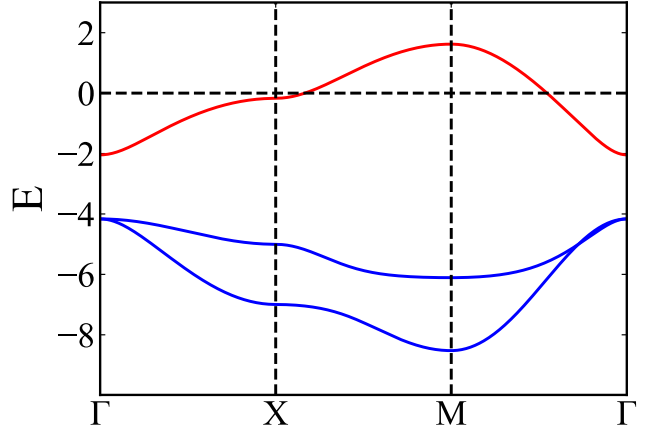


FIG. 1. Electronic band structure of the half-filled Emery model along the high-symmetry directions $\Gamma \rightarrow X \rightarrow M \rightarrow \Gamma$ in the Brillouin zone of the square lattice with the 1MTO hopping parameters and $\Delta_{dp} = 2$. The high-symmetry points are defined as $\Gamma = (0, 0)$, $X = (\pi, 0)$ and $M = (\pi, \pi)$. Energy zero corresponds to the Fermi level. The red line represents the target band and the two blue lines show the screening bands.

$$\begin{aligned}
 H = & \sum_{\mathbf{k}, \sigma} c_{\mathbf{k}, \sigma}^\dagger h_0(\mathbf{k}) c_{\mathbf{k}, \sigma} \\
 & + U_{dd} \sum_i n_{i, \uparrow}^d n_{i, \downarrow}^d + U_{pp} \sum_j n_{j, \uparrow}^{p_j} n_{j, \downarrow}^{p_j} \\
 & + U_{dp} \sum_{\langle i, j \rangle, \sigma, \sigma'} n_{i\sigma}^d n_{j\sigma'}^{p_j}, \quad (1)
 \end{aligned}$$

where $c_{\mathbf{k}, \sigma}^\dagger = (d_{\mathbf{k}, \sigma}^\dagger, p_{x, \mathbf{k}, \sigma}^\dagger, p_{y, \mathbf{k}, \sigma}^\dagger)$ is the creation operator for the electrons on $3d_{x^2-y^2}$, $2p_x$ and $2p_y$ orbitals. $h_0(\mathbf{k})$ is the kernel of the noninteracting tight-binding Hamiltonian in momentum space given in Ref. 44. The hopping parameters are chosen to be those of the 1MTO model. The diagonal elements of $h_0(\mathbf{k})$ contain the information about the charge-transfer energy, which is defined as the energy separation between the copper $3d_{x^2-y^2}$ orbital and the oxygen $2p$ orbital, $\Delta_{dp} = \varepsilon_d - \varepsilon_p$. In this study, we report all energies in eV.

The half-filled noninteracting band structure for $\Delta_{dp} = 2$ is plotted in Fig. 1 along some specific high-symmetry directions in the Brillouin zone of the square lattice. The half-filled upper band (red line) which crosses the Fermi level is our low-energy target band and the remaining two fully filled bands (blue lines) are the high-energy bands to be integrated out successively. As can be seen, for the Emery model, the high-energy and low-energy degrees of freedom are well separated by Δ_{dp} , making the procedure to integrate out the high-energy bands well-defined. At the same time, Δ_{dp} is roughly the magnitude of the minimum gap between the target band and the screening bands, which is the main parameter in the polarization

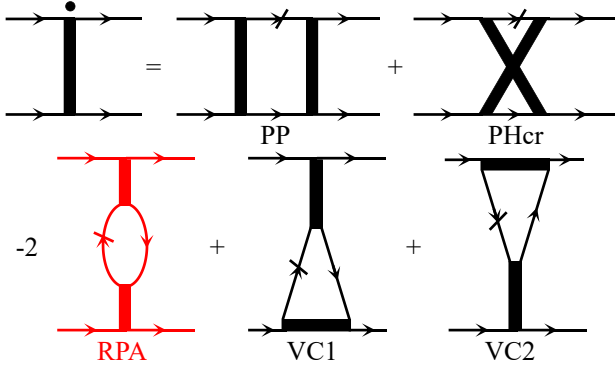


FIG. 2. Diagrammatic representation of the fRG flow equations. The cRPA is equivalent to the red diagram denoted as RPA. The dot over the interaction vertex on the left-hand side of the flow equation denotes the derivative with respect to the cutoff Λ . The internal solid line represents the free propagator and the slashed solid line denotes the corresponding single-scale propagator.

functions and plays an important role during the renormalization process.³²

The interaction term of the Hamiltonian in Eq. (1) is given in real space. Here, the labels i and j run over all Cu and O sites, and $\langle i, j \rangle$ denotes the summation over nearest neighbor Cu-O bonds. The interaction parameters U_{dd} and U_{pp} correspond to the on-site Coulomb repulsion between two electrons with opposite spins located on the Cu $3d$ and O $2p$ orbitals, respectively. The nearest neighbor Cu-O interaction U_{dp} is neglected in many studies but has been shown to be important to stabilize the charge transfer insulating state of the Emery model at half filling.^{44,50} In the following study, we use $U_{dd} = 13$ and $U_{pp} = 7$. The values of Δ_{dp} and U_{dp} will be varied and specified explicitly in the following subsections.

B. cfRG procedure

In this paper, we only study the SU(2)-symmetric case and write the two-particle interaction as

$V_{o_1 o_2; o_3 o_4}^\Lambda(k_1, k_2, k_3, k_4)$, where Λ is the flow parameter. The variables o_i denote orbital indices and $k_i = (\mathbf{k}_i, i\omega_i)$ combined momenta and Matsubara frequencies. The indices 1 and 2 denote the two incoming particles while 3 and 4 denote the two outgoing particles. Here, the SU(2)-symmetry is fulfilled by the requirement that the configuration for the spin indices of the interaction is fixed by the Kronecker delta $\delta_{s_1, s_3} \delta_{s_2, s_4}$, which means the incoming particle 1 and the outgoing particle 3 have the same spin projection and particles 2 and 4 have the same spin projection.³⁷ Since k_4 can be determined by momentum/energy conservation, $k_4 = k_1 + k_2 - k_3$, the two-particle vertex is denoted as $V_{o_1 o_2; o_3 o_4}^\Lambda(k_1, k_2, k_3)$ in the following to abbreviate the notation.

Without self-energy corrections, the SU(2) symmetric flow equations in the level-2 truncation for the two-particle interaction in the cfRG scheme can be obtained by employing the Wick-ordered fRG formalism³² and read as follows:

$$\begin{aligned} \partial_\Lambda V_{o_1 o_2; o_3 o_4}^\Lambda(k_1, k_2, k_3) = & \partial_\Lambda P_{o_1 o_2; o_3 o_4}^\Lambda(k_1, k_3; s) \\ & + \partial_\Lambda D_{o_1 o_2; o_3 o_4}^\Lambda(k_1, k_4; t) + \partial_\Lambda C_{o_1 o_2; o_3 o_4}^\Lambda(k_1, k_3; u), \end{aligned} \quad (2)$$

where the Mandelstam variables are introduced as

$$s = k_1 + k_2, t = k_3 - k_1, u = k_4 - k_1. \quad (3)$$

The three terms on the right-hand side of the flow equation Eq. (2) are called the particle-particle channel (P), the direct particle-hole channel (D) and the crossed particle-hole channel (C), respectively. The expressions are given by (using N for the number of unit cells)

$$\partial_\Lambda P_{o_1 o_2; o_3 o_4}^\Lambda(k_1, k_3; s) = \frac{T}{N} \sum_{\substack{k \\ \tilde{o}_1 \tilde{o}_2; \tilde{o}_3 \tilde{o}_4}} V_{o_1 o_2; \tilde{o}_1 \tilde{o}_2}^\Lambda(k_1, s - k_1, k) \partial_\Lambda [G_{\tilde{o}_1 \tilde{o}_3}^\Lambda(k) G_{\tilde{o}_2 \tilde{o}_4}^\Lambda(s - k)] V_{\tilde{o}_3 \tilde{o}_4; o_3 o_4}^\Lambda(k, s - k, k_3), \quad (4)$$

$$\begin{aligned} \partial_\Lambda D_{o_1 o_2; o_3 o_4}^\Lambda(k_1, k_4; t) = & -\frac{2T}{N} \sum_{\substack{k \\ \tilde{o}_1 \tilde{o}_2; \tilde{o}_3 \tilde{o}_4}} V_{o_1 \tilde{o}_4; o_3 \tilde{o}_1}^\Lambda(k_1, k + t, k_1 + t) \partial_\Lambda [G_{\tilde{o}_1 \tilde{o}_3}^\Lambda(k) G_{\tilde{o}_2 \tilde{o}_4}^\Lambda(k + t)] V_{\tilde{o}_3 o_2; \tilde{o}_2 o_4}^\Lambda(k, k_4 + t, k + t) \\ & + \frac{T}{N} \sum_{\substack{k \\ \tilde{o}_1 \tilde{o}_2; \tilde{o}_3 \tilde{o}_4}} V_{o_1 \tilde{o}_4; o_3 \tilde{o}_1}^\Lambda(k_1, k + t, k_1 + t) \partial_\Lambda [G_{\tilde{o}_1 \tilde{o}_3}^\Lambda(k) G_{\tilde{o}_2 \tilde{o}_4}^\Lambda(k + t)] V_{\tilde{o}_3 o_2; o_4 \tilde{o}_2}^\Lambda(k, k_4 + t, k_4) \\ & + \frac{T}{N} \sum_{\substack{k \\ \tilde{o}_1 \tilde{o}_2; \tilde{o}_3 \tilde{o}_4}} V_{o_1 \tilde{o}_4; \tilde{o}_1 o_3}^\Lambda(k_1, k + t, k) \partial_\Lambda [G_{\tilde{o}_1 \tilde{o}_3}^\Lambda(k) G_{\tilde{o}_2 \tilde{o}_4}^\Lambda(k + t)] V_{\tilde{o}_3 o_2; \tilde{o}_2 o_4}^\Lambda(k, k_4 + t, k + t), \quad (5) \end{aligned}$$

$$\partial_\Lambda C_{o_1 o_2; o_3 o_4}^\Lambda(k_1, k_3; u) = \frac{T}{N} \sum_{\substack{k \\ \tilde{o}_1 \tilde{o}_2; \tilde{o}_3 \tilde{o}_4}} V_{o_1 \tilde{o}_4; \tilde{o}_1 o_4}^\Lambda(k_1, k + u, k) \partial_\Lambda [G_{\tilde{o}_1 \tilde{o}_3}^\Lambda(k) G_{\tilde{o}_2 \tilde{o}_4}^\Lambda(k + u)] V_{\tilde{o}_3 o_2; o_3 \tilde{o}_2}^\Lambda(k, k_3 + u, k_3). \quad (6)$$

The diagrammatic representation of the flow equation is depicted in Fig. 2. The dot over the four-point vertex denotes the derivative with respect to the cutoff Λ and the slashed loop line represents the single-scale propagator, $S^\Lambda = dG_{o_1 o_2}^{(0), \Lambda}/d\Lambda$. Only one type of one-loop diagram is generated for the P channel (PP) and C channel (PHcr). There are three one-loop diagrams for the D channel, one corresponding to the RPA-type diagram (RPA) and the other two to the vertex corrections (VC1, VC2). The cRPA can be reproduced by keeping only the RPA-type series diagram (the red diagram) in the D channel. It is readily seen that the cRG goes beyond cRPA by including more one-loop diagrams and these can produce significant corrections to the cRPA effective interaction.³⁵

In general, the two-particle interaction V^Λ at the energy scale Λ generated by integrating out the high energy bands during the renormalization group flow is a function of spin indices, orbital indices, wave vectors and Matsubara frequencies. The rich information incorporated in this effective interaction might lead to qualitatively different physical effects. For example, the frequency dependent interaction downfolded from the frequency independent bare interactions was shown to be crucial to open up a gap in undoped La_2CuO_4 .⁵⁰ On the other hand, this complexity makes it challenging to perform numerical simulations for realistic multiband systems. To simplify the calculations, we use the intraorbital on-site and instantaneous bilinear interaction approximation of Ref. 34 where the interaction term is represented by

$$\begin{aligned} V_{o_1 o_2; o_3 o_4}^\Lambda(k_1, k_2, k_3) = & P_{o_1 o_2; o_3 o_4}^\Lambda(k_1, k_3; s) + D_{o_1 o_2; o_3 o_4}^\Lambda(k_1, k_4; t) + C_{o_1 o_2; o_3 o_4}^\Lambda(k_1, k_3; u) \\ \simeq & P_{o_1 o_3}^\Lambda(s) \delta_{o_1 o_2} \delta_{o_3 o_4} + D_{o_1 o_2}^\Lambda(t) \delta_{o_1 o_3} \delta_{o_2 o_4} + C_{o_1 o_2}^\Lambda(u) \delta_{o_1 o_4} \delta_{o_2 o_3}. \quad (7) \end{aligned}$$

In this approximation, each channel depends on one collective wave vector and one bosonic Matsubara frequency, s , t or u , respectively. This allows one to understand the D -channel as a potentially retarded interaction between density fermion bilinears. In the intraorbital on-site approximation, the two fermion operators of this bilinear have the same site, orbital and spin index, with the latter being summed over. Yet, the two bilinears coupled by this interaction in the D -channel can differ, i.e. $o_1 \neq o_3$ in the second line above, and hence non-local interactions are captured as well. The C - and P -channel terms can, in the same approximation, be interpreted as potentially retarded spin exchange and pair hopping terms, such that the effective interaction contains on-site and non-local, orbital-dependent density-density, exchange and pair-hopping interactions.

The above equations are written in the orbital basis as the interaction part of the three-band model is given in the orbital basis. However, it is physically much more intuitive to describe the downfolding procedure in the band basis. More specifically, the loop term in the particle-particle channel can be written as

$$\begin{aligned} G_{\tilde{o}_1 \tilde{o}_3}^\Lambda(k) G_{\tilde{o}_2 \tilde{o}_4}^\Lambda(s - k) = & \sum_{n_1, n_2} U_{\tilde{o}_3, n_1}(\mathbf{k}) U_{\tilde{o}_4, n_2}(\mathbf{s} - \mathbf{k}) \\ & \times [G_{n_1}^\Lambda(k) G_{n_2}^\Lambda(s - k)] U_{n_1, \tilde{o}_1}^\dagger(\mathbf{k}) U_{n_2, \tilde{o}_2}^\dagger(\mathbf{s} - \mathbf{k}), \quad (8) \end{aligned}$$

where n_1 and n_2 are band indices and U are the unitary matrices which diagonalize the non-interacting Hamiltonian $h_0(\mathbf{k})$ in Eq. (1). Here, we use the flat-cutoff scheme

where the regulator simply switches off the high-energy bands irrespective of their energy and momentum and the propagator $G_n^\Lambda(k)$ is given by

$$G_n^\Lambda(k) = \begin{cases} \Lambda G_n^{(0)}(k) & \text{for } n \in \text{high-energy bands,} \\ G_n^{(0)}(k) & \text{for } n \in \text{target bands.} \end{cases} \quad (9)$$

The above form of the propagator excludes the contribution from the loop term composed of two target-band propagators as the Λ derivative equals 0 in this case. The effective interaction $V_{o_1 o_2; o_3 o_4}^\Lambda$ in the orbital basis can be obtained by integrating the flow equations from $\Lambda = 1$ down to $\Lambda = 0$. Then, the effective interaction $V_{tt,tt}^\Lambda(k_1, k_2, k_3)$ in the target band denoted by the band index t can be obtained by projections with the orbital-to-band transformation unitary matrices U

$$V_{tt,tt}^\Lambda(k_1, k_2, k_3) = \sum_{o_1 o_2 o_3 o_4} U_{o_1, t}(\mathbf{k}_1) U_{o_2, t}(\mathbf{k}_2) \times V_{o_1 o_2; o_3 o_4}^\Lambda(k_1, k_2, k_3) U_{t, o_3}^\dagger(\mathbf{k}_3) U_{t, o_4}^\dagger(\mathbf{k}_4). \quad (10)$$

The zero-frequency momentum average of this quantity with all high-energy bands removed at $\Lambda = 0$ can be used to define the effective target-band onsite repulsion (see also Refs. 34 and 35)

$$U_{\text{eff}} = \frac{1}{N^3} \sum_{\vec{k}_1, \vec{k}_2, \vec{k}_3} V_{tt,tt}^{\Lambda=0}(k_1, k_2, k_3)|_{s=u=t=0}. \quad (11)$$

In the following, we calculate and compare three different types of effective interactions $V_{o_1 o_2; o_3 o_4}^\Lambda(k_1, k_2, k_3)$ in Eq. (10), which are then used in Eq. (11): the bare interaction, the cRPA-screened interaction and the cfRG interaction. The bare interaction is the unrenormalized interaction projected onto the target band using Eq. (10) with band index t given by the target band. The bare interaction is Matsubara frequency independent as the orbital-to-band transformations are only momentum dependent. Both the cRPA and the cfRG interactions are functions of momenta and Matsubara frequencies as visible from Eq. (7). For the static effective onsite repulsion U_{eff} in Eq. (11), we set all these collective frequencies s , t and u to zero. In principle, even for onsite bare interactions, the projected effective interactions will have nonlocal terms. For the given situation these nonlocal terms will however be rather small, as can be inferred, e.g., from Ref. 34.

Besides the static U_{eff} , we discuss a frequency-dependent $U_{\text{eff}}(\omega_n)$ as

$$U_{\text{eff}}(\omega_n) = \frac{1}{N^3} \sum_{\vec{k}_1, \vec{k}_2, \vec{k}_3} V_{tt,tt}^{\Lambda=0}(k_1, k_2, k_3)|_{s=u=t=\omega_n}. \quad (12)$$

Fixing the total incoming frequency s and the two transfer frequencies t and u to the same value is of course an approximation to the full three-frequency dependence

of the effective interaction. At least, this compromise, introduced in Ref. 34, captures the true frequency dependence in the limit of very small or very large values of these frequencies. Furthermore, for the QMC solution of the effective model within DMFT, this reduction is currently necessary. Below we use DMFT(QMC) to solve the half-filled low-energy effective one-band models with the frequency-dependent cfRG and cRPA effective interactions. The calculations are performed on a 16×16 lattice at a temperature $T = 0.1$.

III. RESULTS

In this section, we calculate the effective interactions in the low-energy target band for the three-band Emery model with cRPA and cfRG as a function of the charge-transfer energy Δ_{dp} and the interatomic $2p$ - $3d$ interaction U_{pd} , in both undoped or doped situations. We begin the discussion with the results for the undoped state, which corresponds to each CuO_2 unit cell occupied by five electrons. We denote this situation by $n = 1$ in the following for simplicity. Subsequently, the electron-doped ($n > 1$) and hole-doped ($n < 1$) cases will be discussed.

A. Frequency and momentum dependence of the effective interactions

As can be seen from the cfRG flow equations, Eq. (2), the downfolded effective interaction will develop rich frequency and momentum structures even for static bare interactions. We show the momentum averaged effective interactions U_{eff} as defined in Eq. (11) as a function of Matsubara frequency for $U_{pd} = 2$, $\Delta_{dp} = 2$ at half filling in the upper panel of Fig. 3. The bare effective interaction without loop corrections is Matsubara frequency independent but lower than the U_{dd} interaction in the three-band model, due to the transformation (11). The cfRG and cRPA results are nontrivial functions of Matsubara frequency ω_n . In the static limit, cfRG and cRPA screen down the bare interaction to less than 80% and this screening effect is slightly stronger in cRPA than that in cfRG. Initially, the cfRG effective interaction is decreasing with increasing ω_n , while the cRPA effective interaction is increasing. However, the frequency dependence of the cfRG effective interaction is non-monotonic and exhibits an upturn around $\omega_n \approx 13$. This non-monotonic behavior of the cfRG interaction is expected, as screening becomes ineffective at high frequencies and both the cfRG and cRPA effective interactions should approach the bare interaction. The maximum at zero frequency in the cfRG interaction can be understood as an effect of the antiscreening C -channel that mixes into the charge channel most strongly at small frequencies. The frequency-dependent effective interaction has been argued to play a crucial role in opening the gap for the insulating state of La_2CuO_4 ⁵⁰ and it shares similar fea-

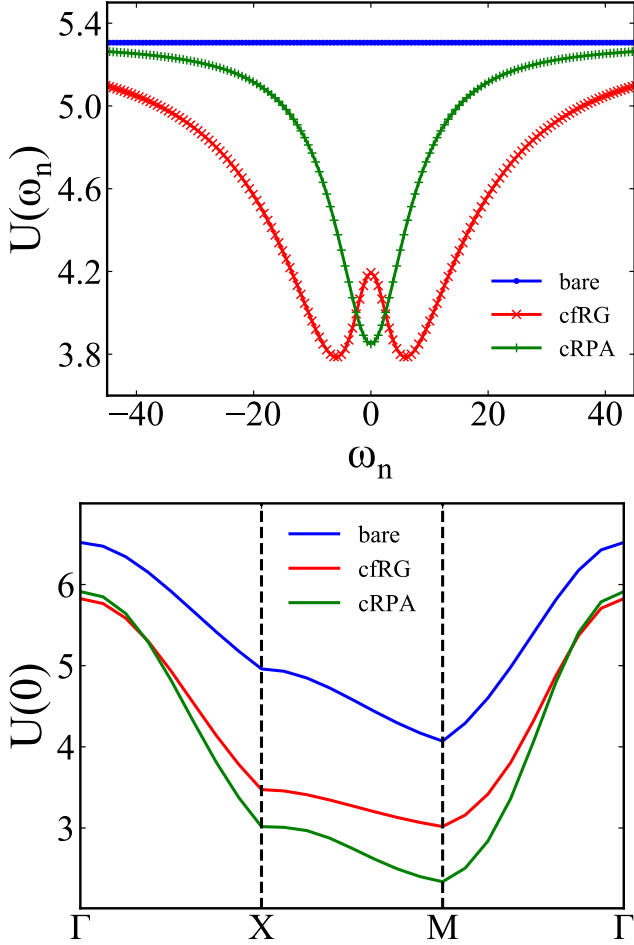


FIG. 3. Upper panel: The frequency dependence of the effective onsite (i.e. momentum averaged) interaction in the target band at the Fermi level. Lower panel: The momentum dependence of the static (zero frequency) effective interaction in the target band. All values are given in units of eVs.

tures within the cuprate family.⁴² Note that the analytic continuation from Matsubara to real frequencies remains a challenging task and is left for future work.

The lower panel of Fig. 3 illustrates the momentum dependence of the zero frequency interactions along the high-symmetry directions of the Brillouin zone. All of the three interactions have a strong momentum dependence with the maximum values at the Γ point. As k moves from $\Gamma = (0,0)$ to $X = (\pi,0)$ and X to $M = (\pi,\pi)$, the interactions decrease and reach the minimum value at M point. Along M to Γ , the opposite behavior is observed. Compared with the bare interaction, the suppression is stronger along X to M and becomes smallest at the Γ point. The overall suppression of the static value is weaker in cfRG than in cRPA.

One main take-away message from these figures is that the differences between the frequency- and momentum dependences of the three interaction types, bare, cRPA and cfRG, is less prominent than the overall suppression

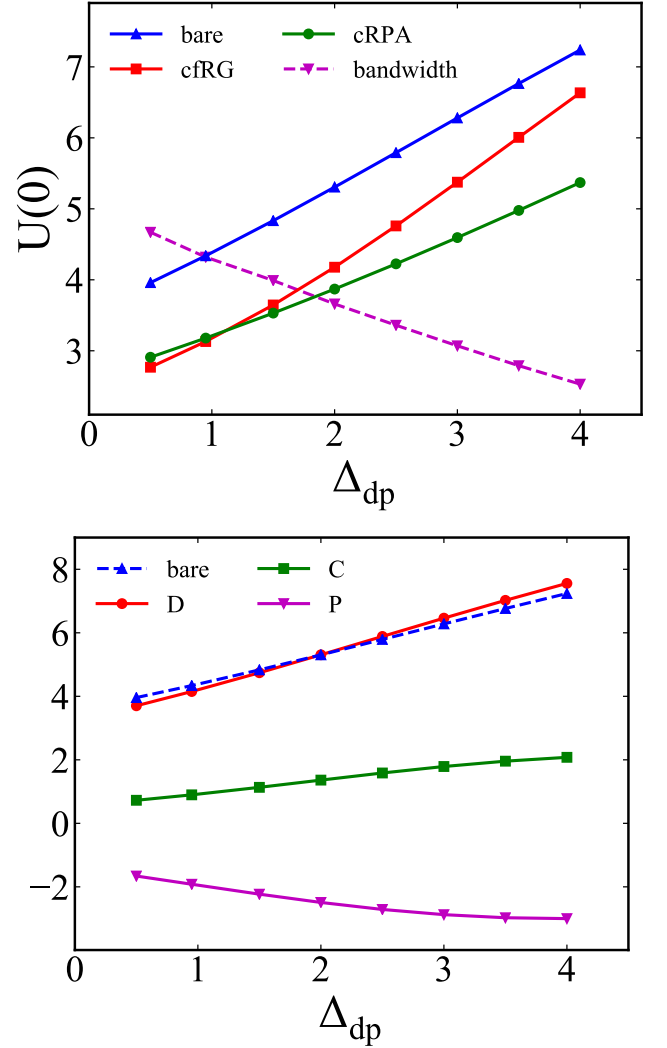


FIG. 4. Upper panel: The effective interaction and the bandwidth of the target band as a function of Δ_{dp} . Lower panel: The channel coupling functions as a function of Δ_{dp} . Data for $U_{dd} = 13$.

effects in cRPA and cfRG. Hence, in a first analysis one can concentrate on the local, zero-frequency effective interaction, the ‘effective U ’.

B. Undoped case for different Δ_{dp} with fixed U_{dp}

The charge-transfer energy Δ_{dp} is one of the key parameters in the Emery model and the value of Δ_{dp} varies substantially between different cuprate families. The strength of the d - p hybridization and the charge (spin) distribution on the CuO_2 layer are controlled by the value of Δ_{dp} . The physical properties of the Emery model have been found to vary fundamentally with Δ_{dp} in the underdoped regime⁵² and even at half-filling.⁵⁶ Moreover, both theoretical and experimental results suggest that Δ_{dp} is anticorrelated with the maximal transition temperature

$T_{c,\max}$ in cuprates,^{38–41} that is, reducing Δ_{dp} yields a larger $T_{c,\max}$. However, it is difficult to determine the accurate value of Δ_{dp} from *ab initio* calculations. As mentioned before, the gap between the low-energy target band and the high-energy screening bands is roughly given by Δ_{dp} . Thus, it is interesting to investigate the screening effect of the Emery model as a function of Δ_{dp} . In this subsection, we set $U_{dp} = 2$ and scan the charge-transfer energy Δ_{dp} .

From the upper panel of Fig. 4, one can clearly see that the screening is slightly stronger for cRG compared to cRPA when $\Delta_{dp} < 1$ and becomes weaker as Δ_{dp} increases. As the values of Δ_{dp} in most of the cuprates families are larger than 1,⁵⁶ overscreening of the static U in the cRPA downfolding scheme is expected for realistic *ab initio* calculations. Screening is less effective for larger Δ_{dp} in cRG, where the effective interaction is screened down to 70% of the bare interaction for the smallest Δ_{dp} and 92% of the bare interaction for the largest Δ_{dp} used in this study. This is consistent with the physical picture that a stronger correlation for the target band is obtained with a larger Δ_{dp} as the d - p hybridization is weaker. However, the ratio of the cRPA effective interaction to the effective bare interaction ($U_{\text{eff}}^{\text{cRPA}}/U_{\text{bare}}$) for different Δ_{dp} remains almost unchanged. Note however that larger Δ_{dp} also implies a narrower conduction band (see Fig. 4), i.e. the effective correlation strength increases even more with Δ_{dp} than what is suggested by the increase of $U(0)$.

According to Eq. (2), the final cRG interaction can be decomposed into the sum of three channels (D, C and P). To gain further insights into the cRG results, we show the three channel coupling functions and the bare interactions in the lower panel of Fig. 4. From this plot we see that both the direct and crossed particle-hole coupling functions are positive while the particle-particle coupling functions are negative for all the Δ_{dp} studied. With increasing Δ_{dp} , the absolute values of the three channel coupling functions increase. The direct particle-hole coupling function is approximately equal to the bare interaction, which implies that the RPA contribution (RPA in Fig. 2) to the screening is almost canceled by the vertex corrections (VC1 and VC2 in Fig. 2). This near-cancellation behavior has also been found in Ref. 35. Since the particle-particle coupling function is more negative than the positive crossed particle-hole coupling function, the bare interaction is screened down in cRG.

C. Undoped case for different U_{dp} with fixed Δ_{dp}

The interatomic $2p$ - $3d$ interaction U_{dp} in the Emery model is often neglected because U_{dp} is small compared to U_{dd} . However, detailed numerical calculations have been performed to argue that in DMFT calculations, the inclusion of U_{dp} , at least at the Hartree level, is crucial to drive a metal-insulator transition of the charge-transfer

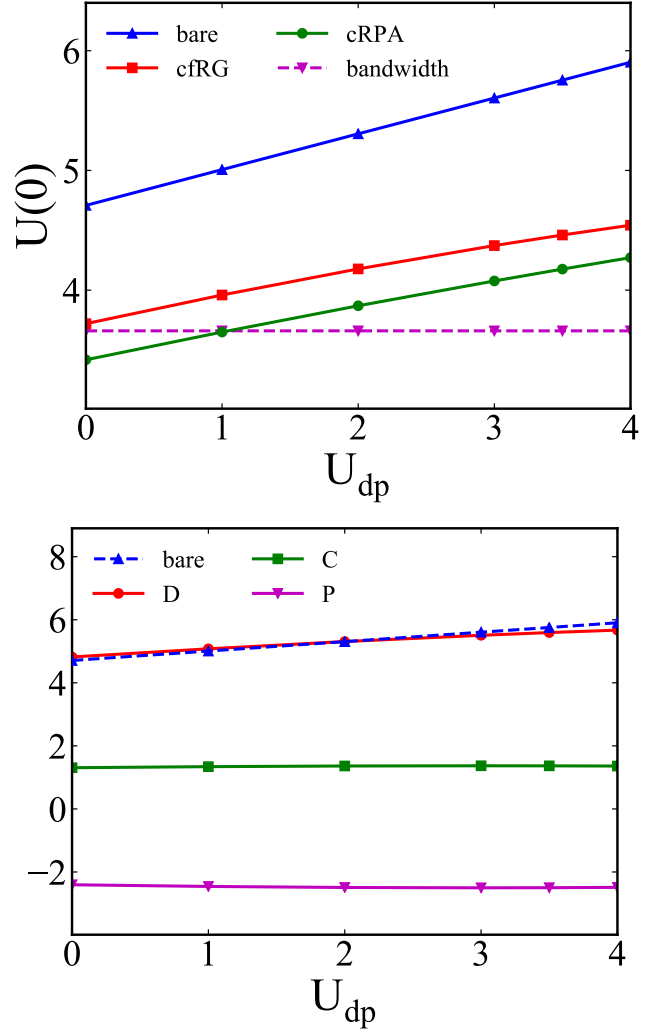


FIG. 5. Upper panel: The effective interaction and the bandwidth of the target band as a function of U_{dp} . Lower panel: The renormalized channel coupling functions as a function of U_{dp} .

type for the Emery model.^{44,50} Furthermore, excitonic fluctuations in the doped cuprates⁴⁶ and photo-induced bandshifts⁴⁷ may also be affected by U_{dp} . In this subsection, we discuss the momentum averaged static effective interactions $U_{\text{eff}}(\omega_n = 0)$ as a function of U_{dp} at half filling for fixed charge-transfer energy $\Delta_{dp} = 2$.

The results are presented in Fig. 5. Here, the reduction of the bare interaction is stronger for cRPA. In contrast to the Δ_{dp} dependence, in both cases, the ratios of the downfolded effective interaction to the bare effective interaction for different U_{dp} are almost the same. Also the width of the conduction band does not depend on U_{dp} .

The overall changes of the effective interactions as a function of U_{dp} are less significant compared to the variation with Δ_{dp} . Our data indicate that larger U_{dp} corresponds to stronger correlations in the low-energy target band. Together with the DMFT result that a charge gap

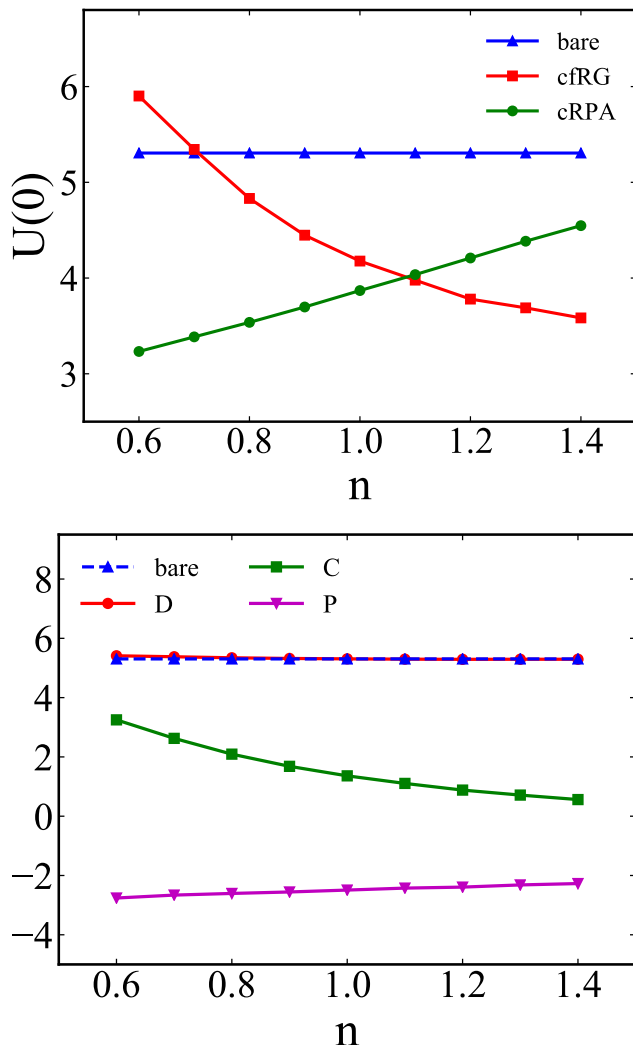


FIG. 6. Upper panel: The effective interaction as a function of doping. Lower panel: The renormalized channel coupling functions as a function of doping. Here we set $U_{dp} = 2$ and $\Delta_{dp} = 2$.

opens in the one-band Hubbard model if the effective interaction goes beyond some critical value,¹⁵ the trend found in Ref. 44 is consistent with our results. In the lower panel of Fig. 5, the three channel coupling functions together with the bare interactions are given. Again, the near-cancellation of the direct particle-hole coupling function is observed. However, the coupling functions in the crossed particle-hole and particle-particle channels are nearly independent of U_{dp} .

D. Doped case for fixed U_{dp} and Δ_{dp}

The doped system is more interesting, since many of the correlation driven exotic phases (pseudogap, strange metal and various density wave states) have been pro-

posed and observed in the doped cuprates.^{53–55} In many numerical studies, the model parameters are treated as independent of doping, however, it should be noted that the values of Δ_{dp} and U_{dp} may change upon doping due to the shift of the O 2p and Cu 3d states.⁵⁸ Accordingly, the values of the effective interactions should change, as discussed in the previous subsections for the undoped cases. To simplify the discussion and focus on the changes of the effective interactions originating from doping, we ignore this effect in this subsection and set $U_{dp} = 2$ and $\Delta_{dp} = 2$.

We show in Fig. 6 the doping dependence of the momentum averaged static effective interactions and the channel decomposed results. Obviously, the bare interaction remains constant as a function of doping since the orbital-to-band transformation matrices are independent of band-filling. In cfRG, the correlation strength is suppressed with increasing filling n , and the crossed particle-hole channel is responsible for this decrease of the effective interaction. This suggests that the correlations are stronger in the hole-doped system compared with the electron-doped system. Similar to our results for the undoped cases, the near-cancellation in the direct particle-hole channel is also found here. Contrary to the crossed particle-particle channel, the effective interaction in the particle-particle channel slightly increases with doping. Besides the direct particle-hole channel, the contributions from the crossed particle-hole channel outweigh the particle-particle channel for $n < 0.7$, which results in the antiscreening effect. Here, the cRPA results follow an opposite trend compared to cfRG as a function of doping. The screening effects become weaker with increasing n . The two downfolded interaction curves cross near $n = 1.1$, below which the effective interaction is stronger for cfRG. In Refs. 42 and 51, the cRPA results suggest that most electron-doped cuprates have a smaller U compared to the hole-doped ones. At first sight, this seems to contradict with our results. However, their results are obtained by doping different parent compounds, which means that different model parameters are used during the calculation. It still remains an experimental challenge to systematically scan the phase diagram from hole doping to electron doping for a single material.⁵⁹

IV. DMFT SOLUTION OF THE LOW-ENERGY MODEL

If the interactions are restricted to the local density-density component, the downfolded single-band models with frequency dependent $U_{\text{eff}}(\omega_n)$ can be solved with DMFT using the techniques developed in Refs. 60 and 61. In DMFT, the lattice system is mapped to an impurity model with a self-consistently determined bath of non-interacting electrons (or hybridization function).¹⁵ An efficient method for solving this impurity model is the hybridization expansion continuous-time Monte Carlo technique,⁶² which expands the partition function of the

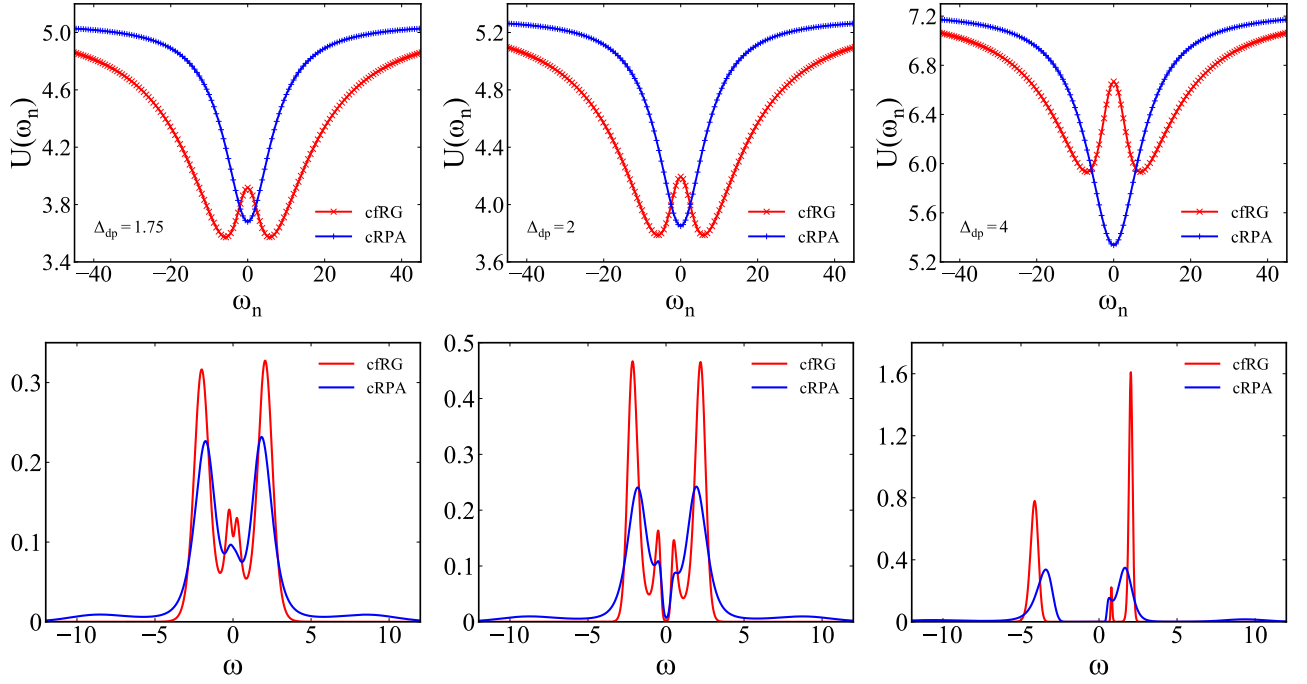


FIG. 7. Effective interactions (top panels) and local spectral functions (bottom panel) for the downfolded single-band models with $\Delta_{dp} = 1.75, 2$, and 4 (from left to right).

Δ_{dp}	$U_{\text{eff}}(0)$ cfRG	$U_{\text{eff}}(0)$ cRPA	bandwidth
1.75	3.92	3.68	3.83
2	4.19	3.85	3.69
2.5	4.78	4.20	3.35
3	5.41	4.57	3.08
4	6.67	5.34	2.54

TABLE I. Static interactions and bandwidths of the downfolded models for different Δ_{dp} .

impurity model in powers of the hybridization function and stochastically samples the corresponding diagrams. In the case of frequency-dependent interactions, all the fermionic creation and annihilation operators in these diagrams are linked by a bosonic function $K(\tau)$, which is the twice integrated retarded interaction,^{63,64}

$$K(\tau) = \frac{1}{\beta} \sum_{n \neq 0} \frac{U_{\text{eff}}(\omega_n) - U_{\text{eff}}(0)}{(i\omega_n)^2} (e^{-i\omega_n \tau} - 1), \quad (13)$$

while the instantaneous interaction is given by the static value $U_{\text{eff}}(0)$. The output of the impurity solver is the impurity Green's function G , which at self-consistency becomes the DMFT approximation to the local lattice Green's function.

In Fig. 7 we plot $U(\omega_n)$ and the resulting DMFT spectral functions $A(\omega) = -\frac{\text{Im}G(\omega)}{\pi}$, obtained with Maximum Entropy analytical continuation,⁶⁵ for three different values of Δ_{dp} . For $\Delta_{dp} = 1.75$, the model is metallic, while for $\Delta_{dp} = 2$ it is a small-gap insulator and for $\Delta_{dp} = 4$ a large-gap insulator. This metal-insulator transition is a

consequence of the Δ_{dp} -dependence of $U_{\text{eff}}(\omega_n)$ and the bandwidth of the low-energy model (Tab. I). It becomes clear though from the upper panels of Fig. 7 that the static values of U_{eff} are not sufficient to quantify the interaction effects, because of the frequency dependence, which is qualitatively different for cfRG and cRPA downfolding. For example, the insulator-metal transition happens at almost the same critical Δ_{dp} for the cfRG and cRPA interactions, despite their substantially different static values, because of the opposite low-energy screening properties (see also Sec. III A). While the static cfRG interaction is larger than the static cRPA interaction, it initially decreases as a function of ω_n , as a result of low-energy anti-screening processes, which are not captured by cRPA. The latter downfolding procedure leads by construction to a monotonically increasing $U_{\text{eff}}(\omega_n)$. Hence, the effective interaction strength in the two downfolded models is comparable, which leads to similar critical Δ_{dp} , while the shape of the spectral functions is different.

A direct measure of the effective interaction strength is the average double occupation $D = \langle n_{\uparrow} n_{\downarrow} \rangle$, which is plotted as a function of Δ_{dp} in Fig. 8. These results confirm that the cRPA and cfRG interactions, if the full frequency dependence is taken into account, produce similar correlation effects. According to this measure, the cfRG interaction is effectively weaker than the cRPA interaction in the vicinity of the insulator-metal transition, despite the larger static values, while it is effectively stronger for $\Delta_{dp} \gtrsim 2.5$.

The frequency dependence of the interaction contains information on the screening processes involving the p

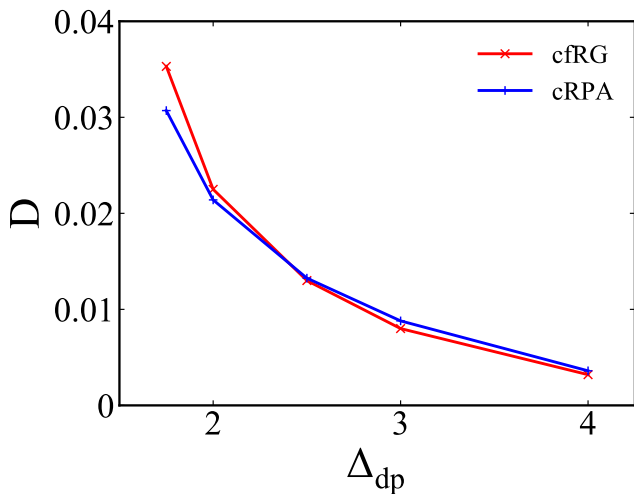


FIG. 8. Double occupancy D as a function of Δ_{dp} .

bands, which propagates into the DMFT solution of the low-energy model. In particular, the spectra obtained with the cRPA interaction feature broad satellites at an energy comparable to the d - p splitting in the original bandstructure, as has been discussed in the context of previous DMFT+ $U_{\text{cRPA}}(\omega)$ studies.^{50,66} The spectrum for the cfRG interaction does not exhibit such satellites, presumably because of the qualitatively different frequency structure with an anti-screening peak around $\omega = 5$ in the real-frequency spectrum $\text{Im}U_{\text{eff}}(\omega)$.

V. SUMMARY

We have presented a study of the downfolded effective interactions for the Emery model by comparing cRPA and cfRG schemes. The momentum and frequency structure was studied and we calculated the effective interactions by scanning the values of the charge transfer gap Δ_{dp} and the interatomic $2p$ - $3d$ interaction U_{pd} at half-filling. By including all five one-loop diagrams in cfRG, we have found significant corrections to cRPA effective interactions for some parameter sets. The static interaction was generically found to be overscreened by cRPA, which suggests that including other one-loop terms and vertex corrections can lead to different predictions. According to our data, the effective interaction increases

as Δ_{dp} increases, and the trend is similar as a function of U_{pd} if one of the parameters is fixed. This indicates that the charge transfer insulating state is stabilized by a larger Δ_{dp} or U_{pd} , which is compatible with the results obtained in Ref. 44. The effective interaction was found to be more sensitive to Δ_{dp} than U_{pd} .

We also studied the doping dependence of the effective interactions. Away from half-filling, the cfRG interaction decreases with increasing particle number mainly due to the decrease of the crossed particle-hole channel, while the opposite trend is observed for cRPA. An antiscreening effect which cannot be captured by cRPA, is found by cfRG in the hole-doped case. For all the cases studied in this paper, a near-cancellation of the direct particle-hole channel is observed.

In the end, it should be noted that the comparison of the two downfolding methods is at the level of the effective interactions. It will be very interesting, in the future, to compare the ground state properties by solving the effective one-band models, which requires advanced numerical methods. We have presented here DMFT results which capture the frequency dependence of the local density-density interactions. These results showed that the effective correlation strength of the cRPA and cfRG downfolded models is actually quite similar, despite the substantial differences in the static values of U . This is the result of an opposite trend in the ω_n -dependence of the interactions. More advanced formalisms are needed to investigate the effect of the non-density-density and nonlocal interactions induced by the downfolding.

Finally, we should mention that the exact downfolding not only produces a frequency-dependent effective interaction, but also a renormalized bare propagator G_0^{cRPA} or G_0^{cfRG} . The bandwidth is usually reduced by self-energy corrections,^{11,45} but the momentum dependence of the renormalization can be nontrivial. These renormalization effects are ignored in our paper. A reduction of the bandwidth would lead to stronger correlations in the low-energy model, which could further enhance the discrepancy between the cfRG and cRPA downfolded models. The investigation of this effect is left for a future study.

ACKNOWLEDGMENTS

CH thanks DFG-RTG 1995 for support. PW acknowledges support from SNSF Grant No. 200021-165539. We thank K. Held and G. Schober for discussions.

¹ W. Kohn and L. J. Sham, *Self-Consistent Equations Including Exchange and Correlation Effects*, Phys. Rev. **140**, A1133 (1965).

² X. Wan, A. M. Turner, A. Vishwanath, and S. Y. Savrasov, *Topological semimetal and Fermi-arc surface states in the*

electronic structure of pyrochlore iridates, Phys. Rev. B **83**, 205101 (2011)

³ N. P. Armitage, E. J. Mele, and A. Vishwanath, *Weyl and Dirac semimetals in three-dimensional solids*, Rev. Mod. Phys. **90**, 015001 (2018).

- ⁴ A. P. Drozdov, M. I. Erements, I. A. Troyan, V. Ksenofontov, and S. I. Shylin, *Conventional superconductivity at 203 K at high pressures*, Nature (London) **525**, 73 (2015).
- ⁵ Y. Li, J. Hao, H. Liu, Y. Li, and Y. Ma, *The metallization and superconductivity of dense hydrogen sulfide*, J. Chem. Phys. **140**, 174712 (2014).
- ⁶ W. E. Pickett, *Electronic structure of the high-temperature oxide superconductors*, Rev. Mod. Phys. **61**, 433 (1989).
- ⁷ M. Imada, A. Fujimori, and Y. Tokura, *Metal-insulator transitions*, Rev. Mod. Phys. **70**, 1039 (1998).
- ⁸ S. Y. Savrasov, G. Resta, and X. Wan, *Local Self-Energies for V and Pd Emergent from a Non-Local LDA+FLEX Implementation*, Phys. Rev. B **97**, 155128 (2018).
- ⁹ H. Sakakibara and T. Kotani, *Model-mapped random phase approximation to evaluate superconductivity in the fluctuation exchange approximation from first principles*, Phys. Rev. B **99**, 195141 (2019).
- ¹⁰ D. Tahara and M. Imada, *Variational Monte Carlo Method Combined with Quantum-Number Projection and Multi-Variable Optimization*, J. Phys. Soc. Jpn. **77**, 114701 (2008).
- ¹¹ M. Imada and T. Miyake, *Electronic Structure Calculation by First Principles for Strongly Correlated Electron Systems*, J. Phys. Soc. Jpn. **79**, 112001 (2010).
- ¹² F. Ma, W. Purwanto, S. Zhang, and H. Krakauer, *Quantum Monte Carlo Calculations in Solids with Downfolded Hamiltonians*, Phys. Rev. Lett. **114**, 226401 (2015).
- ¹³ W. Metzner and D. Vollhardt, *Correlated Lattice Fermions in $d=\infty$ Dimensions*, Phys. Rev. Lett. **62**, 324 (1989).
- ¹⁴ A. Georges and G. Kotliar, *Hubbard model in infinite dimensions*, Phys. Rev. B **45**, 6479 (1992).
- ¹⁵ A. Georges, G. Kotliar, W. Krauth, and M. J. Rozenberg, *Dynamical Mean-Field Theory of Strongly Correlated Fermion Systems and the Limit of Infinite Dimensions*, Rev. Mod. Phys. **68**, 13 (1996).
- ¹⁶ G. Kotliar, S. Y. Savrasov, K. Haule, V. S. Oudovenko, O. Parcollet, and C. A. Marianetti, *Electronic structure calculations with dynamical mean-field theory*, Rev. Mod. Phys. **78**, 865 (2006).
- ¹⁷ E. A. Goremychkin, H. Park, R. Osborn, S. Rosenkranz, J.-P. Castellan, V. R. Fanelli, A. D. Christianson, M. B. Stone, E. D. Bauer, K. J. McClellan, D. D. Byler, and J. M. Lawrence, *Coherent band excitations in CePd_3 : A comparison of neutron scattering and ab initio theory*, Science **359**, 186 (2018).
- ¹⁸ R. Adler, C.-J. Kang, C.-H. Yee, and G. Kotliar, *Correlated materials design: prospects and challenges*, Rep. Prog. Phys. **82**, 012504 (2019).
- ¹⁹ K. G. Wilson, *The renormalization group: Critical phenomena and the Kondo problem*, Rev. Mod. Phys. **47**, 773 (1975).
- ²⁰ F. Aryasetiawan, M. Imada, A. Georges, G. Kotliar, S. Biermann, and A. I. Lichtenstein, *Frequency-dependent local interactions and low-energy effective models from electronic structure calculations*, Phys. Rev. B **70**, 195104 (2004).
- ²¹ T. Miyake, F. Aryasetiawan, and M. Imada, *Ab initio procedure for constructing effective models of correlated materials with entangled band structure*, Phys. Rev. B **80**, 155134 (2009).
- ²² F. Aryasetiawan, K. Karlsson, O. Jepsen, and U. Schönberger, *Calculations of Hubbard U from first-principles*, Phys. Rev. B **74**, 125106 (2006).
- ²³ K. Nakamura, Y. Yoshimoto, T. Kosugi, R. Arita, and M. Imada, *Ab initio Derivation of Low-Energy Model for -ET Type Organic Conductors*, J. Phys. Soc. Jpn. **78**, 83710 (2009).
- ²⁴ T. O. Wehling, E. Şaşıoğlu, C. Friedrich, A. I. Lichtenstein, M. I. Katsnelson, and S. Blügel, *Strength of Effective Coulomb Interactions in Graphene and Graphite*, Phys. Rev. Lett. **106**, 236805 (2011).
- ²⁵ E. Şaşıoğlu, C. Friedrich, and S. Blügel, *Effective coulomb interaction in transition metals from constrained random-phase approximation*, Phys. Rev. B **83**, 121101(R) (2011).
- ²⁶ L. Vaugier, H. Jiang, and S. Biermann, *Hubbard U and Hund exchange J in transition metal oxides: Screening versus localization trends from constrained random phase approximation*, Phys. Rev. B **86**, 165105 (2012).
- ²⁷ M. Casula, P. Werner, L. Vaugier, F. Aryasetiawan, T. Miyake, A. J. Millis, and S. Biermann, *Low-Energy Models for Correlated Materials: Bandwidth Renormalization from Coulombic Screening*, Phys. Rev. Lett. **109**, 126408 (2012).
- ²⁸ H. Shinaoka, M. Troyer, and P. Werner, *Accuracy of downfolding based on the constrained random-phase approximation*, Phys. Rev. B **91**, 245156 (2015).
- ²⁹ Q. Han, B. Chakrabarti, and K. Haule, *Investigation into the inadequacy of cRPA in reproducing screening in strongly correlated systems*, arXiv:1810.06116
- ³⁰ M. Hirayama, T. Tadano, Y. Nomura, and R. Arita, *Materials design of dynamically stable d^9 layered nickelates*, Phys. Rev. B **101**, 075107 (2020).
- ³¹ H. Sakakibara, S. W. Jang, H. Kino, M. J. Han, K. Kuroki, and T. Kotani, *Model-Mapped RPA for Determining the Effective Coulomb Interaction*, J. Phys. Soc. Jpn. **86**, 044714 (2017).
- ³² C. Honerkamp, *Effective interactions in multiband systems from constrained summations*, Phys. Rev. B **85**, 195129 (2012).
- ³³ M. Kinza and C. Honerkamp, *Low-energy effective interactions beyond the constrained random-phase approximation by the functional renormalization group*, Phys. Rev. B **92**, 045113 (2015).
- ³⁴ C. Honerkamp, *Efficient vertex parametrization for the constrained functional renormalization group for effective low-energy interactions in multiband systems*, Phys. Rev. B **98**, 155132 (2018).
- ³⁵ C. Honerkamp, H. Shinaoka, F. F. Assaad, and P. Werner, *Limitations of constrained random phase approximation downfolding*, Phys. Rev. B **98**, 235151 (2018).
- ³⁶ V. J. Emery, *Theory of high- T_c superconductivity in oxides*, Phys. Rev. Lett. **58**, 2794 (1987).
- ³⁷ M. Salmhofer and C. Honerkamp, *Fermionic renormalization group flows: Technique and theory*, Prog. Theor. Phys. **105**, 1 (2001).
- ³⁸ C. Weber, C. Yee, K. Haule, and G. Kotliar, *Scaling of the transition temperature of hole-doped cuprate superconductors with the charge-transfer energy*, Europhys. Lett. **100**, 37001 (2012).
- ³⁹ W. Ruan, C. Hu, J. Zhao, P. Cai, Y. Peng, C. Ye, R. Yu, X. Li, Z. Hao, C. Jin, X. Zhou, Z.-Y. Weng, and Y. Wang, *Relationship between the parent charge transfer gap and maximum transition temperature in cuprates*, Sci. Bull. **61**, 1826 (2016).
- ⁴⁰ D. Rybicki, M. Jurkutat, S. Reichardt, C. Kapusta, and J. Haase, *Perspective on the phase diagram of cuprate high-temperature superconductors*, Nat. Commun. **7**, 11413 (2016).

- ⁴¹ M. Zegrodnik, A. Biborski, M. Fidrysiak, and J. Spalek, *Superconductivity in the three-band model of cuprates: Variational wave function study and relation to the single-band case*, Phys. Rev. B **99**, 104511 (2019).
- ⁴² F. Nilsson, K. Karlsson, and F. Aryasetiawan, *Dynamically screened Coulomb interaction in the parent compounds of hole-doped cuprates: Trends and exceptions*, Phys. Rev. B **99**, 075135 (2019).
- ⁴³ J. Zaanen, G. A. Sawatzky, and J. W. Allen, *Band gaps and electronic structure of transition-metal compounds*, Phys. Rev. Lett. **55**, 418 (1985).
- ⁴⁴ P. Hansmann, N. Parragh, A. Toschi, G. Sangiovanni, and K. Held, *Importance of d-p Coulomb interaction for high T_C cuprates and other oxides*, New J. Phys. **16**, 033009 (2014).
- ⁴⁵ M. Hirayama, Y. Yamaji, T. Misawa, and M. Imada, *Ab initio effective Hamiltonians for cuprate superconductors*, Phys. Rev. B **98**, 134501 (2018).
- ⁴⁶ M. Hirayama, T. Misawa, T. Ohgoe, Y. Yamaji, and M. Imada, *Effective Hamiltonian for cuprate superconductors derived from multiscale ab initio scheme with level renormalization*, Phys. Rev. B **99**, 245155 (2019).
- ⁴⁷ D. Golez, M. Eckstein, and P. Werner, *Multiband nonequilibrium GW+EDMFT formalism for correlated insulators*, Phys. Rev. B **100**, 235117 (2019).
- ⁴⁸ M. Dvorak and P. Rinke, *Dynamical configuration interaction: Quantum embedding that combines wave functions and Green's functions*, Phys. Rev. B **99**, 115134 (2019).
- ⁴⁹ T. Ohgoe, M. Hirayama, T. Misawa, K. Ido, Y. Yamaji, and M. Imada, *Ab initio study of superconductivity and inhomogeneity in a Hg-based cuprate superconductor*, Phys. Rev. B **101**, 045124 (2020).
- ⁵⁰ P. Werner, R. Sakuma, F. Nilsson, and F. Aryasetiawan, *Dynamical screening in La_2CuO_4* , Phys. Rev. B **91**, 125142 (2015).
- ⁵¹ S. W. Jang, H. Sakakibara, H. Kino, T. Kotani, K. Kuroki, and M. J. Han, *Direct theoretical evidence for weaker correlations in electrondoped and Hg-based hole-doped cuprates*, Sci. Rep. **6**, 33397 (2016).
- ⁵² A. Chiciak, E. Vitali, H. Shi, and S. Zhang, *Magnetic orders in the hole-doped three-band Hubbard model: Spin spirals, nematicity, and ferromagnetic domain walls*, Phys. Rev. B **97**, 235127 (2018).
- ⁵³ P. A. Lee, N. Nagaosa, and X.-G. Wen, *Doping a Mott insulator: Physics of high-temperature superconductivity*, Rev. Mod. Phys. **78**, 17 (2006).
- ⁵⁴ B. Keimer, S. A. Kivelson, M. R. Norman, S. Uchida, and J. Zaanen, *From quantum matter to high-temperature superconductivity in copper oxides*, Nature (London) **518**, 179 (2015).
- ⁵⁵ E. Fradkin, S. A. Kivelson, and J. M. Tranquada, *Colloquium: Theory of intertwined orders in high temperature superconductors*, Rev. Mod. Phys. **87**, 457 (2015).
- ⁵⁶ E. Vitali, H. Shi, A. Chiciak, and S. Zhang, *Metal-insulator transition in the ground state of the three-band Hubbard model at half filling*, Phys. Rev. B **99**, 165116 (2019).
- ⁵⁷ S. Acharya, C. Weber, E. Plekhanov, D. Pashov, A. Taraphder, and M. Van Schilfgaarde, *Metal-Insulator Transition in Copper Oxides Induced by Apex Displacements*, Phys. Rev. X **8**, 021038 (2018).
- ⁵⁸ T. Xiang, H. G. Luo, D. H. Lu, K. M. Shen, and Z. X. Shen, *Intrinsic electron and hole bands in electron-doped cuprate superconductors*, Phys. Rev. B **79**, 014524 (2009).
- ⁵⁹ J. Orenstein and A. Vishwanath, *Breaking through to the other side*, Nat. Phys. **6**, 655 (2010).
- ⁶⁰ P. Werner and A. J. Millis, *Efficient DMFT-simulation of the Holstein-Hubbard Model*, Phys. Rev. Lett. **99**, 146404 (2007).
- ⁶¹ P. Werner and A. J. Millis, *Dynamical Screening in Correlated Electron Materials*, Phys. Rev. Lett. **104**, 146401 (2010).
- ⁶² P. Werner, A. Comanac, L. De Medici, M. Troyer, and A. J. Millis, *Continuous-Time Solver for Quantum Impurity Models*, Phys. Rev. Lett. **97**, 076405 (2006).
- ⁶³ T. Ayral, S. Biermann, and P. Werner, *Screening and Non-local Correlations in the Extended Hubbard Model from Self-Consistent Combined GW and Dynamical Mean Field Theory*, Phys. Rev. B **87**, 125149 (2013).
- ⁶⁴ P. Werner and M. Casula, *Dynamical screening in correlated electron systems - from lattice models to realistic materials*, Journal of Physics: Condensed Matter **28**, 383001 (2016).
- ⁶⁵ <https://bitbucket.org/lewinboehnke/maxent>
- ⁶⁶ P. Werner, M. Casula, T. Miyake, F. Aryasetiawan, A. J. Millis, and S. Biermann, *Satellites and large doping- and temperature-dependence of electronic properties in hole-doped BaFe_2As_2* , Nat. Phys. **8**, 331-337 (2012).